

# Nanostructured gadolinium-doped ceria microsphere synthesis from ion exchange resin: Multi-scale in-situ studies of solid solution formation

Marie Caisso <sup>a,g</sup>, Florent Lebreton <sup>a</sup>, Denis Horlait <sup>a</sup>, Sébastien Picart <sup>b</sup>, Philippe M. Martin <sup>c</sup>, René Bès <sup>c</sup>, Catherine Renard <sup>d</sup>, Pascal Roussel <sup>d</sup>, Daniel R. Neuville <sup>e</sup>, Kathy Dardenne <sup>f</sup>, Jörg Rothe <sup>f</sup>, Thibaud Delahaye <sup>a,\*</sup>, André Ayrat <sup>g</sup>

<sup>a</sup> CEA, DEN, DTEC/SDTC/LEMA, F-30207 Bagnols-sur-Cèze Cedex, France

<sup>b</sup> CEA, DEN, DRCP/SERA/LCAR, F-30207 Bagnols-sur-Cèze Cedex, France

<sup>c</sup> CEA, DEN, DEC/SESC/LLCC, F-13108 Saint-Paul-Lez-Durance Cedex, France

<sup>d</sup> Unité de Catalyse et Chimie du Solide, UMR 8012 CNRS, Ecole Nationale Supérieure de Chimie de Lille BP 90108, 59652 Villeneuve d'Ascq Cedex, France

<sup>e</sup> Institut de Physique du Globe de Paris-CNRS, Géochimie & Cosmochimie, 1 rue Jussieu, 75005 Paris, France

<sup>f</sup> Karlsruhe Institute of Technology, Institute for Nuclear Waste Disposal (KIT-INE), Hermann-von-Helmholtz-Platz 1, D-76344 Eggenstein-Leopoldshafen, Germany

<sup>g</sup> Institut Européen des Membranes, UMR 5635 CNRS-ENSCM-UM2, CC047, Université Montpellier 2, F-34095 Montpellier Cedex 5, France

## ARTICLE INFO

## ABSTRACT

In the current nano sized material revolution, the main limitations to a large scale deployment of nanomaterials involve health concerns related to nano dissemination via air. Developing new chemical routes benefiting from nano size advantages while avoiding their hazards could overcome these limitations. Addressing this need, a chemical route leading to soft nano particle agglomerates, i.e., macroscopic precursors presenting the ability to be decomposed into nano sized materials, was developed and applied to  $\text{Ce}_{0.8}\text{Gd}_{0.2}\text{O}_{2-\delta}$ . Using cerium/gadolinium loaded ion exchange resin, the  $\text{Ce}_{0.8}\text{Gd}_{0.2}\text{O}_{2-\delta}$  solid solution formation as a function of temperature was studied in situ through X ray diffraction, X ray absorption spectroscopy and Raman spectroscopy. Temperatures corresponding to the organic skeleton decomposition and to the mixed oxide crystallization were identified. An optimal heat treatment, leading to nanostructured soft agglomerates, was established. Microsphere processing capabilities were evaluated and particle size distribution measurements were recorded. A very low fracture strength was calculated, and a nanometric particle size distribution (170 nm) was determined.

### Keywords:

GDC  
XAS  
Raman  
XRD  
Nanostructured  
Ion exchange resin

## 1. Introduction

Nanomaterials are often considered a technological break through that can improve materials' performance or give them new properties [1], such as new optical, electronic or magnetic properties [2,3]. Although their synthesis is now well controlled, their use in fabrication processes remains very complicated due to the risk of spread [4,5]. These risks increase operating cost through the mandatory use of dedicated tools such as glove boxes or clean rooms and in some cases prevent any possibility of utilization [6,7]. Using soft agglomerated nanoparticles can overcome this limitation

or contribute to less restrictive processes. With that in mind, an innovative chemical route based on ion exchange resin was established. The solution proposed here is not to agglomerate previously synthesized nanoparticles but to synthesize nanostructured and calibrated microspheres which can be decomposed into nano scale powder by pelletizing or milling, for example.  $\text{Ce}_{0.8}\text{Gd}_{0.2}\text{O}_{2-\delta}$  nanostructured microsphere synthesis was selected to illustrate this new route.

Currently, the most studied anode material for Solid Oxide Fuel Cell (SOFC) applications is the Ni YSZ (nickel and yttria stabilized zirconia) cermet (ceramic metal) composite. This composite fulfills a majority of the requirements for an efficient anode, such as high catalytic activity and good electrical conductivity, as well as excellent structural and microstructural integrity under operating conditions. However, its high catalytic activity also induces a major

\* Corresponding author. Tel.: +334 6679 6542.

E-mail address: thibaud.delahaye@cea.fr (T. Delahaye).

drawback due to the presence of Ni. Ni catalyzes the formation of carbon deposits from hydrocarbons under reducing conditions [8]. To solve this problem, gadolinium doped ceria (GDC) is frequently used as a substitute for YSZ in the Ni-YSZ cermet [9,10]. This mixed conductor is known to suppress coke formation, and its catalytic behavior in steam reforming of methane has been reported in several studies [11,12]. GDC can also be used on the cathode side (air side) to form a cermet (ceramic-ceramic) composite electrode (e.g.,  $\text{Pr}_{0.58}\text{Sr}_{0.4}\text{Fe}_{0.8}\text{Co}_{0.2}\text{O}_{3-\delta}$  GDC composite air electrode) [13]. For such SOFC applications, the synthesis of GDC as porous nanostructured microspheres would be of great interest as precursors for screen printing. Indeed, such soft agglomerates present the ability to be decomposed into nanoparticles during the tri-cylinder milling step required to form a slurry for electrode screen printing [14]. Electrode screen printing will be thus facilitated and gas diffusion to triple phase boundaries improved after electrode sintering.

In a very different context, GDC compounds can be used as non-radioactive surrogates for the  $\text{U}_{1-x}\text{Am}_x\text{O}_{2\pm\delta}$  mixed oxides, called AmBB (Am bearing blankets) and identified as possible targets for Am transmutation. Transmutation of Am into stable or short-lived elements in fast neutron reactors [15] would be a promising option, currently studied to reduce nuclear waste radiotoxicity. However, AmBB dense pellet fabrication requires special attention due to the high radiotoxicity of Am [16]. Currently, the fabrication of these pellets is based on powder metallurgy processes with ball milling steps which generate large amounts of fine radioactive particles [17–20]. Dustless processes which eliminate the use of such fine and highly contaminating powders during pellet production are thus mandatory before envisaging an industrial deployment. In this aim, the development of an innovative route using micrometric spherical precursors is studied. Through an adaptation of the weak acid resin (WAR) process [21–25], the general approach consists of elaborating micrometric and brittle spherical mixed oxide precursors. This geometry was chosen to facilitate the filling of the compaction chamber and subsequent pelletizing. After pelletizing, similar to nanostructured microspheres, obtained pellets are composed of highly reactive nanoparticles allowing for a low sintering temperature. A first step in the demonstration of the feasibility of this process is the use of lanthanide surrogates for uranium and americium, cerium and gadolinium, respectively, as they have chemical properties similar to these actinides [26] and allow many experiments to be performed at lower cost.

Meeting needs of the two above discussed scientific domains, the development of a spherule route called the calcined resin microsphere pelletizing (CRMP) process has been initiated. In the first part, resin loading with a selected Ce/Gd ratio of 80/20 is described. In the second part, in situ high temperature characterizations by TGA (thermogravimetric analysis), XRD (high temperature X-ray diffraction), XAS (X-ray absorption spectroscopy) and Raman spectroscopy of the loaded resin are detailed. These experiments were used to identify the temperature steps (organic skeleton removal steps, crystallization), helping to determine the optimal calcination conditions required to synthesize the target mixed oxide. It also allowed the chemical environment of the cations in the resin and in the oxide to be studied, revealing the evolution of the oxidation degree of lanthanide elements during their mineralization. The oxide microspheres obtained with this process were also characterized by EDS (energy dispersive spectrometry) to measure the obtained Ce/Gd ratio and by SEM (scanning electron microscopy), to observe their microstructure in order to apprehend their future processing behavior. The viability of pelletizing nanostructured microspheres was studied through microsphere pressing and the determination of their fracture strength. Finally, microsphere milling with a tri-cylinder device led to a slurry with nanometric particle size distribution.

## 2. Experimental

### 2.1. Precursors

The employed polyacrylic resin comes from The Dow Chemicals Company (Rohm and Haas, Chauny, France) and consists of an IMAC HP333 gel type acrylic exchanger in the form of micro-spherical beads. Concentrated ammonia solution (25%, Merck, Pro Analysis) and concentrated nitric acid solution (64%, Fisher Chemical, certified ACS Plus) were used in their diluted form (1 M) as washing solutions for resin preparation. Hexahydrate cerium(III) nitrate ( $\text{Ce}(\text{NO}_3)_3 \cdot 6\text{H}_2\text{O}$ , 99.99% purity, Merck) and hexahydrate gadolinium nitrate ( $\text{Gd}(\text{NO}_3)_3 \cdot 6\text{H}_2\text{O}$ , 99.99% pure, Prolabo) were employed to prepare solutions for resin loading.  $\text{H}_2\text{O}$  stoichiometry of each nitrate was determined by thermogravimetry prior to use.

### 2.2. Resin metal loading

A batch of microspheres with a 630–800  $\mu\text{m}$  diameter distribution was washed in a column by successive circulation of 1 M aqueous nitric acid solution, deionized water, 1 M aqueous ammonia solution, and finally deionized water, then repeating the complete cycle a second time. This protocol was employed to remove cationic and chemical impurities potentially present in the pores of the microspheres after their industrial synthesis, as well as to convert the resin to its ammonium form. Pre-loading the acrylic resin (protonated form) with labile ammonium ions ( $\text{NH}_4^+$ ) is a necessary step before cationic loading because it fixes the lanthanide ions in substitution for ammonium ions. The resin was then poured into a column with deionized water. In parallel, a 0.5 L aqueous solution of the selected lanthanide elements in stoichiometric proportions was prepared from cerium and gadolinium nitrates in order to get a Ce/Gd ratio equal to 80/20. This stock solution was recirculated through the column filled with the resin batch as long as fixation occurs, i.e., for approximately 16 h. This time was deduced from pH monitoring of the solution showed in Fig. 1, the loading end corresponding to the stabilization of the pH value. After loading, the resin was washed with deionized water, drained under vacuum and finally dried in an oven at 393 K for 12 h.

### 2.3. Room temperature characterizations

The Ce/Gd ratio of the stock solution and dissolved resin was determined by inductively coupled plasma atomic emission

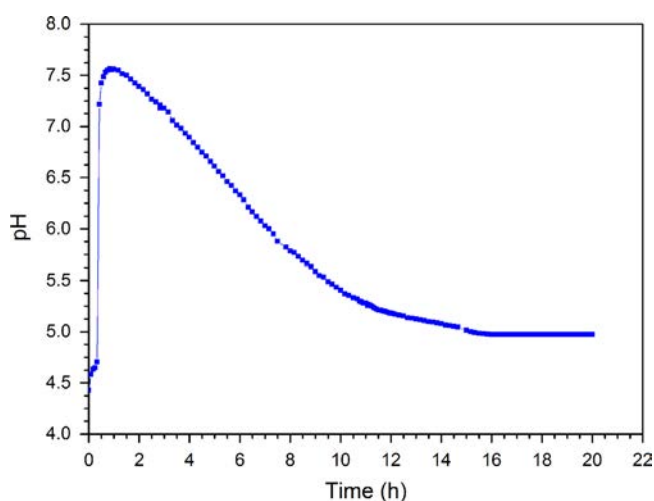


Fig. 1. pH evolution of the (Ce/Gd) solution during resin loading. pH decreases during the experiment from the progressive increase of  $[\text{NH}_4^+]$  in solution. The stabilization of pH over 16 h indicates the completion of the cationic exchange.

spectroscopy (ICP AES) using ACTIVA HORIBA LAB equipment. XRD measurement was done on compounds using a Bruker D8 Advance apparatus with a Cu  $K\alpha_{1,2}$  radiation and equipped with a linear Lynx Eye detector, in a  $\theta/\theta$  configuration. The step was of  $0.02^\circ$  with an integral time of 0.34 s per step, for an angular domain of  $20$  to  $80^\circ 2\theta$ . The lattice parameter of the synthesized solid solution was determined using the FullprofSuite software [27], with a Le Bail method for refinement [28].

#### 2.4. In situ monitoring of resin calcination

Thermogravimetric analyses (TGA) and differential scanning calorimetry (DSC) analyses were performed to identify the key temperatures corresponding to the organic matter departure, with STA 449C Netzsch equipment. The resin beads were placed in an alumina crucible and calcined at 1773 K under flowing air, at a heating rate of  $1.5 \text{ K min}^{-1}$ .

The employed diffractometer was a Bruker D8 Advance device also operating under Cu  $K\alpha_{1,2}$  radiation, using a Vantec detector and an Anton Paar HTK1200N furnace, in a  $\theta/\theta$  configuration. In situ XRD was performed under air on a 150 mg batch of resin ground to powder and spread on an alumina sample holder. The sample was heated at about  $1.5 \text{ K min}^{-1}$  up to 1373 K. A  $20$  to  $50^\circ 2\theta$  angular domain was chosen to observe the appearance and evolution of the main peaks of the oxide. The chosen step size was  $0.02^\circ$  with an integral time of 0.34 s per step. From 293 K to 1073 K, diagrams were recorded every 25 K, and every 50 K from 1073 K to 1373 K. The above described method was used for lattice parameter refinement, while the crystallite size was determined through integral breadth methods by Halder Wagner Langford analysis [29]. The instrumental resolution function was calibrated using a  $\text{LaB}_6$  NIST standard.

In parallel, in situ XAS measurements were performed at the INE (Institute for Nuclear Waste Disposal) beamline [30,31] of the ANKA synchrotron facility (Kalsruhe Institute of Technology, Germany) under dedicated operating conditions (2.5 GeV, 120–150 mA). A Si(111) double crystal monochromator coupled with collimating and focusing Rh coated mirrors was used for energy selection. The incident ( $I_0$ ) intensity was measured with an ionization chamber. The fluorescence photons were measured using a Si solid state detector. During measurements, the temperature of the sample was controlled using a microfurnace in which the sample holder, which is also the heating element, consists of a 1 mm diameter Pt/Ir (10%) wire with a 0.5 mm hole at its midpoint [32,33]. In situ XAS measurements were performed on a single spherule inserted in the hole. The spectra were recorded at the Ce  $L_{III}$  edge (5723 eV), focused on the XANES (X ray absorption near edge structure) only. Energy calibration was performed with respect to the first inflection point of a Cr metal foil XANES spectrum (5989.0 eV) collected before and after the in situ experiment.  $\text{Ce}^{+IV}$  and  $\text{Ce}^{+III}$  reference spectra were collected at RT on  $\text{CeO}_2$  and  $\text{Ce}(\text{NO}_3)_3$  samples respectively, using transmission pellets prepared with commercial pure compounds.

After a first RT measurement, a temperature cycle was performed, composed of successive isothermal plateaus at 400 K, 500 K, 620 K and 1070 K. During each of these plateaus, at least two 25 min spectra were recorded. No significant deviations were observed between spectra at a given temperature. The furnace measurement chamber was under a static air atmosphere during the whole experiment. XANES spectra were normalized using linear functions for pre and post edge modeling. White line maximum and inflection point ( $E_0$ ) positions were taken as the first zero crossing of the first and second derivatives, respectively. Pre edge removal and normalization were performed using ATHENA software [34,35].

The third in situ characterization of the solid solution formation was carried out through Raman spectroscopy analysis. The same microfurnace as that used for in situ XAS measurements was used, following the same thermal treatment under air. Spectra were recorded using a T64000 Jobin Yvon Horiba confocal triple micro Raman spectrometer equipped with a CCD detector. The wavelength used for sample excitation was 488 nm, extracted from an Innova C5 Ar laser. For the in situ experiment, the laser power was attenuated 100 times, and three acquisition cycles of 180 s were performed for each selected temperature from  $10 \text{ cm}^{-1}$  to  $1200 \text{ cm}^{-1}$ .

#### 2.5. Thermal treatment

This part of the study was dedicated to the establishment, based on the previous observations, of an optimal thermal treatment leading to a controlled microstructure. This heat treatment was applied to a batch of resin beads in a tubular furnace (Nabertherm, HTRH 100 300) under synthetic air flow (Air Liquide, 20%  $\text{O}_2$  80%  $\text{N}_2$ ). The chemical composition of the beads was determined through the measurement of the Ce/Gd ratio by ICP AES analyses. This analysis was done by dissolving the oxide in an acidic medium ( $4 \text{ M HNO}_3 + 0.5 \text{ M H}_2\text{O}_2$ ). The microstructure of the oxide batch was also characterized and open/closed porosity ratios were determined after mineralization, using experimental apparent and effective densities along with the theoretical density. In addition, obtained results were correlated with observations of the microstructure and the porosity inside the oxide microspheres. Thus, scanning electron microscopy (SEM FEG) was performed on both the surface and the bulk of the microspheres using a Supra 55 ZEISS instrument.

#### 2.6. Standard characterizations

Characterizations were also carried out on the resin and oxide microspheres. Effective density, including open porosity, was measured by helium pycnometry (Accupyc 1330 Micrometrics pycnometer) equipped with a  $1 \text{ cm}^3$  sample module. Apparent density of microspheres was determined by volume and mass measurements on a sample holder containing a layer of a few hundred beads. The number of spheres and the batch volume were estimated from image analysis using optical video photography and the Ellix pattern recognition software. These measurements were done on oxide microspheres to determine the sphere size distribution and open/closed porosity ratios. The oxide microspheres were also ground in a solvent (terpineol) to be turned into slurry using a tri cylinder miller. Particle size distribution measurements were performed on the obtained slurry with a Malvern laser Mastersizer2000 analyzer. Single oxide microspheres were pressed with an instrumented Instron low load micropress to test their ability to be pressed into pellets during pelletizing. The fracture strength value can be deduced from these measurements.

### 3. Results and discussion

#### 3.1. Characterization of the loaded resin

##### 3.1.1. Determination of the cerium/gadolinium ratio in the resin

The stock solution presented the desired (80/20) ratio, before and after loading, indicating that the fixation was congruent: no selectivity from the resin was observed between the two considered cations. Concerning the beads, the 80/20 target ratio is also reached, confirming the results for the solution. Microspheres coming from this single batch were used for all subsequent

characterizations, assuring that all the results can be related to initial (80/20) loaded resin beads.

### 3.1.2. TGA analysis

The thermal conversion of 50 mg of loaded resin was investigated using TGA at a heating rate of  $1.5 \text{ K min}^{-1}$  from room temperature (RT) to 1773 K under air. Fig. 2 (top) presents the sample relative weight and calorific evolution during heating. TGA analysis shows a main weight loss between 400 K and 600 K, corresponding to a massive organic phase departure. The slow slope at the beginning represents a stage when mostly water is leaving the structure and when carbon oxidation begins. Around 600 K, an important exothermic DSC peak is visible, typical of a chemical transformation or a phase transition. In this case, it is correlated with the combustion of organic matter, corresponding to an energy release concomitant with the onset of crystallization. Above this temperature, a small linear weight decrease with temperature can be noticed, corresponding presumably to the equilibration of the  $\text{O}_2$  content inside the compound according to the  $p\text{O}_2$  and residual carbon departure. Concerning the DSC signal over 600 K, variations might be attenuated by the intense exothermic peak described previously. Another TGA/DSC measurement, presented in Fig. 2 (bottom) was thus performed on a sample previously pre treated up to 600 K in the TGA and which had thus already lost the majority of its carbon content, corresponding to the 400 K 600 K weight loss. This allowed variations beyond this temperature to be measured more accurately, notably for DSC measurements. Due to this protocol, two calorimetric variations are

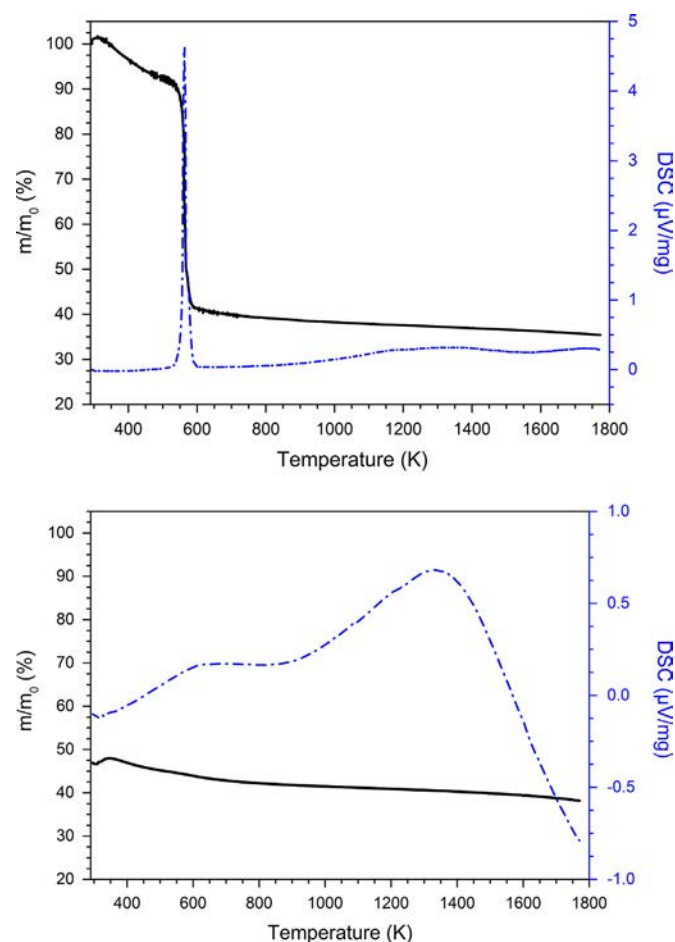


**Fig. 2.** On the left, thermogravimetric and DSC analysis performed under air, showing the weight loss of the loaded resin as a function of temperature; on the right thermogravimetric and DSC analysis performed under air on pre-treated loaded resin up to 600 K.

revealed from 600 K to 1000 K and around 1350 K. The first one may be attributed to the beginning of crystallization after carbon departure, releasing energy during the stabilization of the system. The second one could attest to a higher energy release that could be related to crystallite growth, a phenomenon that comes at higher temperature after global oxide formation. Such an interpretation could be confirmed by XRD and Raman spectroscopy results.

### 3.1.3. XRD analysis

The residue of the thermal conversion inside the TGA apparatus was analyzed by XRD (Fig. 3). The sample appears to be mono phasic, as a single set of peaks corresponding to a single crystal structure is evidenced. This phase is attributed to fluorite type structure with a lattice parameter equal to  $5.425(1) \text{ \AA}$ . This value, which is higher than that of cerium dioxide ( $5.411 \text{ \AA}$ ) [36], is explained by the presence of gadolinium in substitution for cerium [37,38], the ionic radius of the substitute cation being bigger than that of the host ( $^{\text{VIII}}\text{R}_{\text{Ce}^{4+}} = 0.970 \text{ \AA}$  and  $^{\text{VIII}}\text{R}_{\text{Gd}^{3+}} = 1.053 \text{ \AA}$ ) [39]. Besides, since gadolinium is only trivalent, its presence generates oxygen vacancies, ensuring the electroneutrality of the structure but also increasing the lattice parameter [40–42]. Taking into account oxygen vacancies, the solid solution formula can be written as  $\text{Ce}_{0.8}\text{Gd}_{0.2}\text{O}_{1.9}\square_{0.1}$ .

## 3.2. In situ monitoring of calcination

### 3.2.1. XRD

The most relevant XRD diagrams showing the oxide crystallization are presented in Fig. 4. At room temperature and up to 523 K, the sample remains amorphous. Above 548 K, three very broad peaks appear. With increasing temperature, the peaks narrow while their relative intensity increases. Starting at 723 K, the peaks are still broad, but a symmetric shape is obtained, indicating that within the limits of XRD sensitivity, a sole solid solution is achieved at this temperature. At 998 K and above, the three relevant diffraction lines are sharp, clearly indicating the presence of only one solid solution. Their profiles and positions are consistent with the presence of a single  $\text{CeO}_2$  based fluorite type structure. This is confirmed by the diffractogram recorded at room temperature on a larger angular domain after the thermal cycle. A lattice parameter of  $5.426(1) \text{ \AA}$  is obtained from the latter, close to that previously determined after calcination and in the literature for this solid solution [43]. The

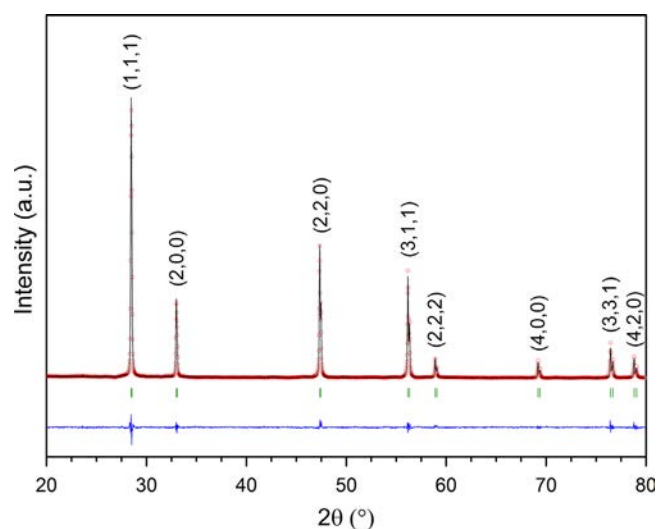


**Fig. 3.** XRD diagram recorded on the powdered residue after TGA measurements and refinement results. Background and  $K\alpha_2$  contributions are removed with the EVA Diffrac<sup>plus</sup> software. Experimental data is in black; the calculated diagram is in red; the difference between them is in blue; Bragg positions are presented in green.

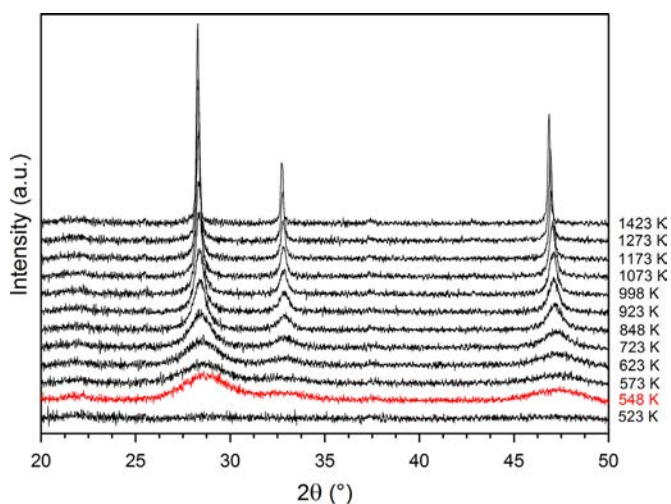


**Fig. 4.** High-temperature X-ray diffraction patterns showing formation of fluorite-type  $\text{Ce}_{0.8}\text{Gd}_{0.2}\text{O}_{1.9}$  solid solution—spectra are not normalized. In red, the temperature at which crystallization begins.

crystallite size determination gives a value of 90(10) nm. This result is close to mixed oxides elaborated via oxalate precursors whose size is around 75 nm at the same temperature [44]. It thus indicates that despite the initial highly porous resin bead structure, the scattered oxidized cations are able to coalesce into fairly large crystallites. This might be helped by the specific surface area of  $15 \text{ m}^2 \text{ g}^{-1}$ , which guarantees a good reactivity of the system.

To summarize, the onset of crystallization is detected by XRD between 523 K and 548 K, which agrees with the temperature of organic phase departure identified by TGA in the previous section. A single solid solution is presumably obtained starting at 723 K and completely formed by 1000 K, temperature at which the peaks become sharp enough for refinement. This property is of particular interest in the case of sintering, during which the presence of secondary phases is generally detrimental. It was notably shown in several actinide/lanthanide mixed oxides that the reaction between the phases to form a solid solution could compete with densification, thereby delaying the latter [45–47].

### 3.2.2. XAS analysis: XANES

Fig. 5 presents the XANES spectra at the Ce  $L_{III}$  edge for the most relevant temperatures, between RT and 1073 K. Spectra of  $\text{Ce}^{+III}$  and  $\text{Ce}^{+IV}$  reference compounds are also reported in Fig. 5 for comparison and are consistent with those previously reported in the literature [48]. RT and 398 K spectra show only one absorption band around 5725 eV with a shoulder near 5735 eV, whereas the higher temperatures reveal the formation of doublet bands, shifted to higher energies (between 5730 eV and 5740 eV). Table 1 summarizes the activation energy values ( $E_0$ ), the white line values (WL) and the ratios of  $\text{Ce}^{+III}$  and  $\text{Ce}^{+IV}$ , obtained by linear combinations of the two reference spectra.

At RT, the XANES spectrum profile indicates the majority presence of trivalent Ce. At 400 K, the cerium is also still mainly trivalent, as the white line maximum is at 5725,9(3) eV, close to the 5726,1(3) eV value of the  $\text{Ce}^{+III}$  reference shown in Table 1. However, the slight shift toward higher energy can already attest to the appearance of a small quantity of  $\text{Ce}^{+IV}$ , as well as the presence of the shoulder at higher energies which does not appear for the  $\text{Ce}^{+III}$  reference. Moreover, linear combinations of the two references shows a 27% and 26%  $\text{Ce}^{+IV}$  contribution in the sample spectra, respectively for RT and 400 K, confirming the presence of  $\text{Ce}^{+IV}$ . This partial oxidation might be explained by the drying step applied to the resin

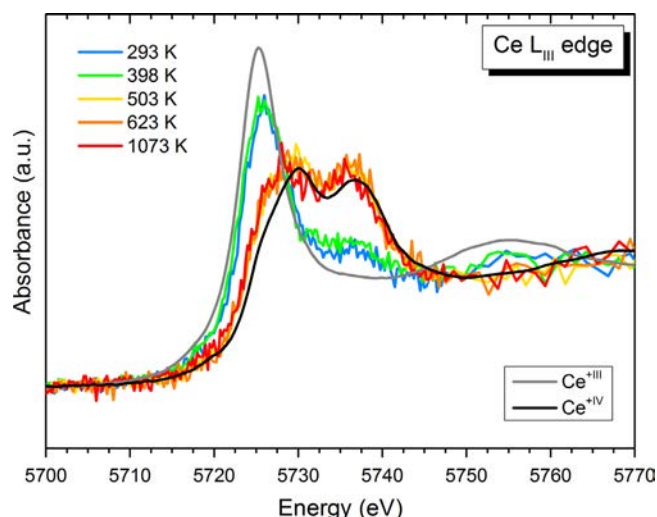


**Fig. 5.** Normalized XANES spectra of the Ce–Gd loaded resin microspheres at several temperatures under air.

**Table 1**

Experimental values of  $E_0$ , WL and mole fractions of  $\text{Ce}^{+III}$  and  $\text{Ce}^{+IV}$  extracted from XANES sample and reference spectra.

$T$ (K)	$E_0$ (eV)	WL (eV)	Mole fractions (at%)	
			$\text{Ce}^{+III}$	$\text{Ce}^{+IV}$
293	5723.1(3)	5726.0(3)	74 (2)	26 (2)
398	5723.9(3)	5725.9(3)	73 (2)	27 (2)
503	5723.8(3)	5729.8(3)	0 (2)	100 (2)
623	5724.1(3)	5728.9(3)	0 (2)	100 (2)
1073	5723.8(3)	5728.2(3)	0 (2)	100 (2)
Ref $\text{Ce}^{+III}$	5722.7(3)	5726.1(3)	100 (2)	0 (2)
Ref $\text{Ce}^{+IV}$	5724.6(3)	5729.9(3)	0 (2)	100 (2)

microspheres after loading, which was performed for 12 h at 393 K in a furnace. Absorption spectra at 503 K and 1073 K indicate the completion of cerium oxidation to  $\text{Ce}^{+IV}$ . Indeed, the emergence of two absorption bands and the similarity of white line values and of the curve profile to those of the  $\text{Ce}^{+IV}$  reference confirm the modification of the Ce oxidation state.

To summarize, XANES results give evidence of the oxidation of  $\text{Ce}^{+III}$  to  $\text{Ce}^{+IV}$  between RT and 503 K. They thereby provide supplementary information about the mineralization mechanism. Significant amounts of  $\text{Ce}^{+IV}$  were detected as low as 398 K, even though most of the organic matter is still present and the oxide long range crystalline structure is not yet formed. The comparison of XAS and XRD results thus suggests that oxide formation and the early stages of crystallization occur simultaneously with or just after the oxidation of cerium. One has to keep in mind that XRD requires a threshold quantity of oxide with a minimum size of coherent domains to induce a diffraction signal that can be distinguished from background.

### 3.2.3. $\mu$ Raman results

Raman in situ experiments were carried out on a single resin bead. Interpretable spectra were only obtained up to 973 K, as temperature induced black body radiation saturates the CCD detector at higher temperatures. Fig. 6 shows spectra at the most relevant temperatures. Significant evolutions of spectra patterns were observed with the temperature increase between RT and 973 K. Between RT and 398 K, the acquired spectra are similar, though noise progressively diminishes with increasing temperature. Limited evolution is then observed up to 573 K. On the several bands observed

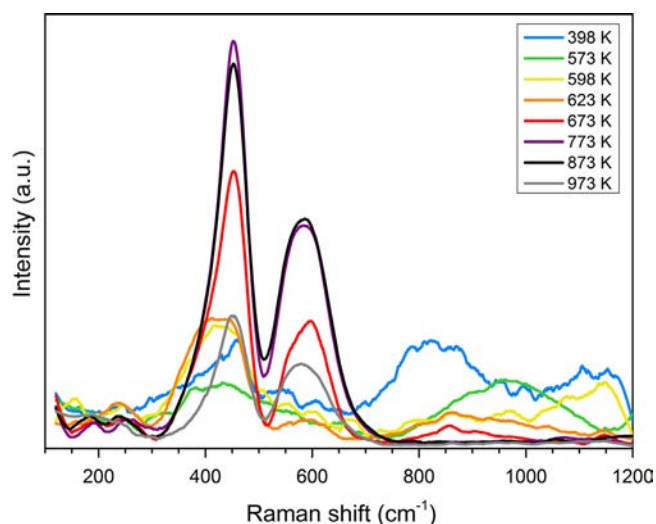


**Fig. 6.** Raman spectra recorded during in-situ experiments of Ce-Gd loaded resin microspheres.

for these low temperatures (398 K and 573 K spectra in Fig. 6) those centered at points over  $600\text{ cm}^{-1}$  could not be precisely identified, though an educated guess could likely attribute them to carbon and oxygen bonds ( $\nu(\text{O}-\text{O})$   $845-900\text{ cm}^{-1}$ ;  $\nu(\text{C}-\text{C})$   $600-1300\text{ cm}^{-1}$  [49]), in other words to the organic skeleton of the resin. From 573 K to 673 K, the relative intensities of these bands decrease until they disappear. This observation thus appears to be in agreement with TGA analysis, as most of the organic matter is found to have been evacuated at such temperatures.

A broad and noisy band centered around  $400-470\text{ cm}^{-1}$ , asymmetric on the low wavenumber side, is observed above 398 K. This band progressively sharpens and becomes more symmetrical up to 673 K. It is not, however, ascertained that it represents the same mode throughout the experiment. From literature data on fluorite  $\text{Ce}_{1-x}\text{Ln}_x\text{O}_{2-x/2}$ , a Raman mode is expected to be active within this wavenumber range. This mode,  $F_{2g}$ , corresponds to the vibration of M-O bonds in a fluorite type structure, i.e., with the M cation (here Ce or Gd) at the center of an  $\text{MO}_8$  cube [41,42,50-52]. On  $\text{CeO}_2$ , this mode is expected to lead to a symmetrical peak centered at  $465\text{ cm}^{-1}$  [53]. For  $\text{Ln}^{+III}$  doped ceria with a fluorite structure, this  $F_{2g}$  mode tends to be shifted to lower wavenumbers compared with  $\text{CeO}_2$  [41,42,50], as a consequence of shortened M-O bonds with  $\text{Ln}^{+III}$  doping, as evidenced through EXAFS investigations [54]. The observation at and over 673 K of a fairly symmetrical band centered at  $455(5)\text{ cm}^{-1}$  accounts for the formation of a  $\text{Ce}_{1-x}\text{Gd}_x\text{O}_{2-x/2}$  solid solution with a long range ordered fluorite structure.

Additionally, it is well reported that for crystallite sizes below 10-20 nm, the lower the crystallite size, the larger the  $F_{2g}$  mode shift to lower wavenumbers and the greater the band asymmetry on its left side [55]. The spectra at 598 K and 623 K correspond to this description. The observed bands whose apexes are at  $430(10)\text{ cm}^{-1}$  presumably correspond to fluorite type oxide nanodomains.

A second band is observed around  $580(5)\text{ cm}^{-1}$  from 623 K (though its presence at 598 K cannot be excluded). Its intensity progressively increases up to 773 K and seems to saturate at 973 K. On fluorite structured  $\text{Ce}_{1-x}\text{Ln}_x\text{O}_{2-x/2}$ , such a band is commonly attributed to a combination of  $A_{1g}$  and  $F_{2g}$  M-O vibration modes in the cubic environment of the fluorite structure presenting at least one oxygen vacancy [41,42,51,52]. This band intensity is related to the amount of oxygen vacancies in the structure, while that of the  $\sim 455\text{ cm}^{-1}$  band is not. The intensity ratio  $I_{580}/I_{455}$  thus increases with the amount of oxygen vacancies, i.e., with the  $\text{Ln}^{+III}$  content in the ceria host structure [41,42,50,56,57]. The observation in Table 2 of the relative increase of this band intensity thus accounts for the

**Table 2**

Experimental values of  $I_{455}$  and  $I_{580}$  from Raman spectra for temperatures from 623 K, significant for oxygen vacancy band existence and the calculated  $I_{580}/I_{455}$  ratio.

T (K)	$F_{2g}$ M-O Raman shift ( $\text{cm}^{-1}$ )	$A_{1g}$ - $F_{2g}$ M-O Raman shift ( $\text{cm}^{-1}$ )	$I_{A_{1g}-F_{2g}}/I_{F_{2g}}$ (%)
623	423(1)	595(1)	22
673	451(1)	596(1)	45
773	452(1)	583(1)	55
873	453(1)	586(1)	60
973	452(1)	577(1)	63

progressive incorporation of  $\text{Gd}^{+III}$  and of associated oxygen vacancies in the  $\text{CeO}_2$  structure between 598 (or 623) and 773 K, reaching a maximum concentration between 773 K and 973 K. This appears to be in full agreement with XRD results since a final fluorite type  $\text{Ce}_{0.8}\text{Gd}_{0.2}\text{O}_{1.9}$  solid solution was suspected at 723 K and definitively observed at 998 K, and also with DSC results in which an exothermic signal was measured from 600 K to 1000 K, presumably corresponding to improved crystallization.

In summary, in situ Raman spectroscopy shows that an oxide with a fluorite structure is formed concomitantly with organic matter departure. At higher temperature, the crystallinity of the oxide progressively increases during  $\text{Ce}_{0.8}\text{Gd}_{0.2}\text{O}_{1.9}$  solid solution formation through oxygen vacancy formation. Finally, crystallization is almost achieved around 750 K and complete above 1000 K according to XRD.

### 3.2.4. General conclusion on solid solution formation

Comparison of results collected from TGA, DSC, XRD, Raman spectroscopy and XAS analyses allows different steps during the formation of  $\text{Ce}_{0.8}\text{Gd}_{0.2}\text{O}_{1.9}$  oxide to be distinguished, as summarized in Fig. 7. Raman experiments show the progressive disappearance of noisy bands between 400 K and 673 K attributed to organic bonds. In the meantime, TGA reveals that organic matter leaves the matrix between 400 K and 600 K. From XAS analysis, the transition from  $\text{Ce}^{+III}$  to  $\text{Ce}^{+IV}$  is recorded between 400 K and 500 K. XRD and Raman spectroscopy concur on the formation of oxide nanodomains during or just after organic matter departure. This data is consistent with the fact that isolated metal oxygen bonds become predominant when organic matter has left the structure, though an extended crystal matrix is not instantaneously formed. That is why a crystalline organization with the fluorite type structure is detected above 500 K by XRD, and the existence of a solid solution is evidenced starting at 700 K. Similarly, DSC and Raman spectroscopy show the formation of nanodomains of  $\text{Ce}_{1-x}\text{Gd}_x\text{O}_{2-x/2}$  oxide below 600 K. Then Raman spectroscopy results show the concomitant improvement of crystallinity and the progressive incorporation of Gd in the  $\text{CeO}_2$  host structure, the latter process finishing below 1000 K, leading to the completion of the target  $\text{Ce}_{0.8}\text{Gd}_{0.2}\text{O}_{1.9}$  solid solution. At and above 1000 K, oxide grains continue to grow as temperature increases, provoking a crystallite size increase of up to 90(1) nm at 1373 K.

### 3.3. Determination of a heat treatment for solid solution formation

The next step in this study was the definition of a possible thermal treatment allowing for the synthesis of a controlled microstructure oxide, optimized for its target applications. Knowing that the organic skeleton leaves the structure between 400 K and 600 K, a temperature range where the oxide also starts to crystallize, a heat treatment was designed, influenced by a previous study on calcination conditions for resin beads [25]. It was evidenced that low heating rates were required to obtain an oxide retaining the precursor's spherical shape. When polymer leaves the microsphere

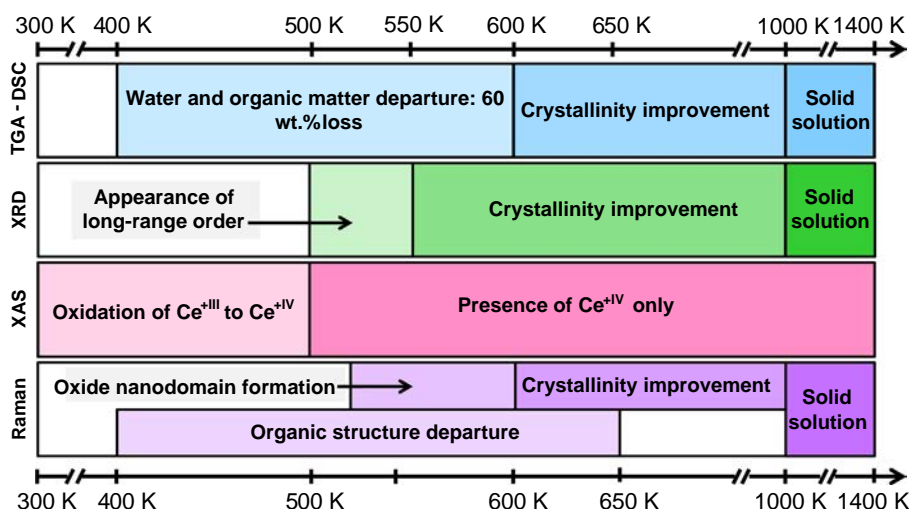


Fig. 7. Summary of the phenomena identified with TGA, XRD, XAS and Raman spectroscopy leading to the formation of the  $\text{Ce}_{0.8}\text{Gd}_{0.2}\text{O}_{1.9}$  solid solution.

in a gaseous state, large porosities can appear and weaken the structure of the bead. Thus, a heating rate of  $1.5 \text{ K min}^{-1}$  from 293 K to 600 K, then of  $5 \text{ K min}^{-1}$  until 1073 K, was selected to prevent microsphere destruction during mineralization. Furthermore, the in situ study of the solid solution formation confirms that it is completed at 1000 K. The maximal temperature was also determined from a previous study on microsphere calcination, where 1073 K was the optimal temperature at which spheres are robust enough to be manipulated and to flow. If the microsphere is mineralized at higher temperatures, the open porosity ratio of the microspheres becomes too low [58], which is a major drawback for the selected applications. This parameter is directly linked to high surface reactivity and good sinterability. The first is required for GDC conductors in SOFC applications, whereas the second is necessary for AmBB fabrication. All these considerations led to the heat treatment presented in Fig. 8.

### 3.4. Characterization of the oxide microspheres

#### 3.4.1. Porosity ratios and Ce Gd content in the oxide

After mineralization, the porosity of the treated microspheres was measured. 66(1)% was open porosity and 3(1)% closed porosity, corresponding to a very low apparent density of 31% TD. The open porosity ratio is presumably high because of the evacuation of the organic phase, which generates significant porosity in the bead skeleton, compounded with the initial porosity of the resin microsphere. Moreover, the maximum measured temperature of 1073 K is below the reported sintering onset temperature for GDC [43], implying that this open porosity is not eliminated by the heat treatment. This agrees with the low expectations for the mechanical resistance of the oxide bead, possibly unsuitable for pelletizing or screen printing.

#### 3.4.2. SEM analysis

The general sphericity of the bead is conserved after the thermal treatment. Bead sphericity guarantees a good flowability useful for both SOFC (e.g. screen printing) and nuclear applications (e.g. pelletizing). SEM observations were performed on the oxide beads, at the surface and along fracture surfaces or cracks. The micrographs are presented in Fig. 9. Porosities are located throughout the sphere, and a porous microstructure consistent with the determined porosity ratios can be identified. This porous oxide microstructure can be correlated with a large reactive surface area required for applications like GDC conductors for SOFC, which also need a consequent porous network to allow gas diffusion during mixed conductor reactions.

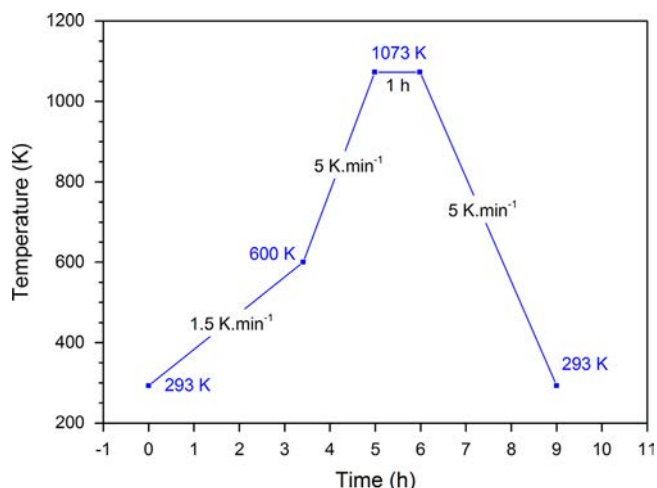


Fig. 8. Thermal treatment for the mineralization of loaded Ce/Gd resin beads.

#### 3.4.3. Microsphere pressing

As previously stated, the interest of this innovative chemical route is to synthesize nanostructured oxide microspheres which will decompose into nanoparticles under applied mechanical stress. Fig. 10 shows, for a single microsphere, the evolution of the applied force as a function of the upper punch displacement for compression test. The maximum strength corresponds to the first crack inside the microsphere and is equal to 41(1) mN. The fracture strength can be determined from the measured ultimate tensile strength using an estimation of the microsphere compression surface calculated in a previous study of similar compounds [58]. The low value calculated, 2.2 (5) MPa, confirms that oxide microspheres are good candidates for pelletizing.

#### 3.4.4. Particle size distribution

To characterize nanoparticles formed after microsphere decomposition, particle size distribution measurements were performed on a slurry obtained from microsphere tricylinder milling in terpineol. Fig. 11 presents the particle size distribution and demonstrates that the obtained powder is nanometric and highly mono dispersed. No signals associated with microspheres were evidenced. Microspheres were all decomposed into nanoparticles during the tri cylinder milling step. These results illustrate the possibility of easy conversion of an

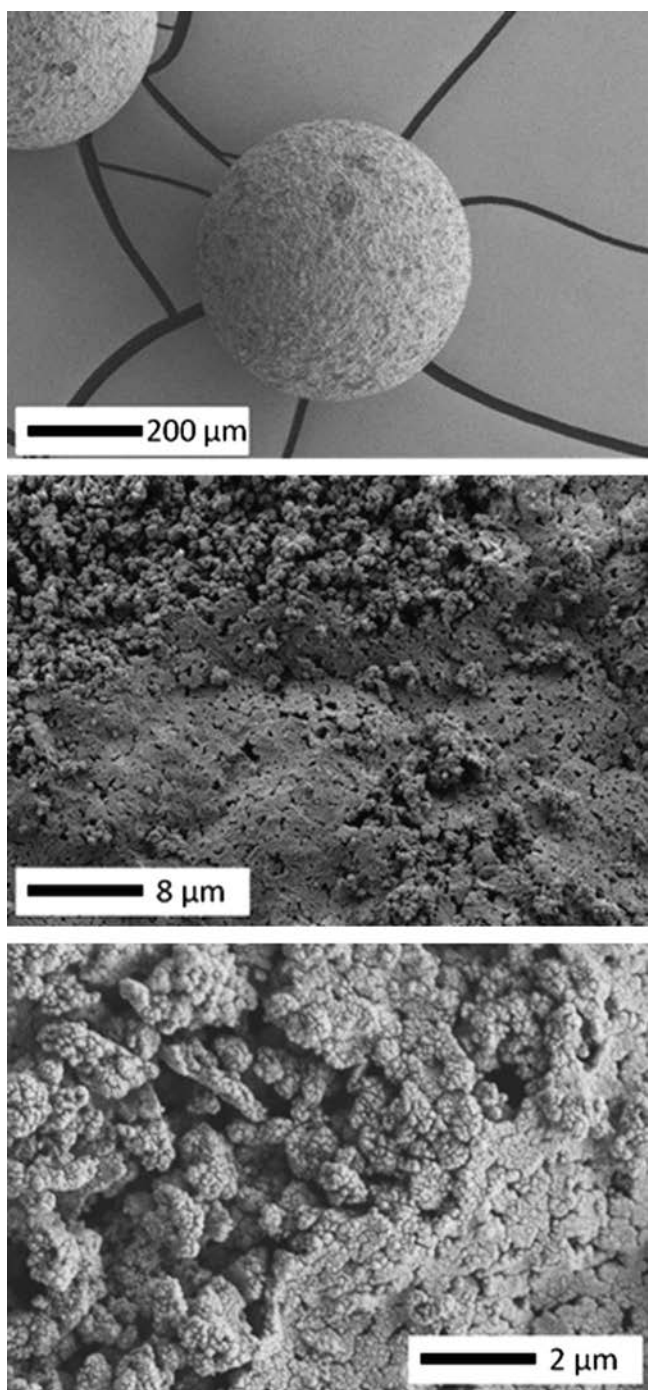


Fig. 9. Secondary-electron SEM micrographs showing the oxide microsphere morphology and microstructure obtained after calcination at 1073 K.

oxide microsphere precursor to a nanoparticle agglomerate form, without the drawbacks of conventional nanoparticle processing.

#### 4. Conclusion

The fabrication of microsphere precursors convertible into soft oxide nanoparticle agglomerates was studied and validated during this work. The formation of  $Ce_{0.8}Gd_{0.2}O_{1.9}$  solid solution via ion exchange resin microsphere calcination was investigated in order to assess the feasibility of new nanostructured soft agglomerates that could be used as synthesized in several processes. The ion loaded resin conversion with the oxidation of the organic phase was

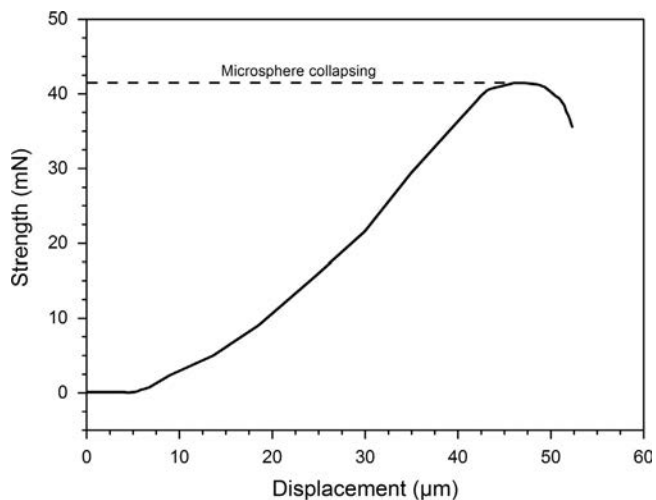


Fig. 10. Experimental curve showing the applied force on the oxide microsphere and corresponding displacement of the upper punch.

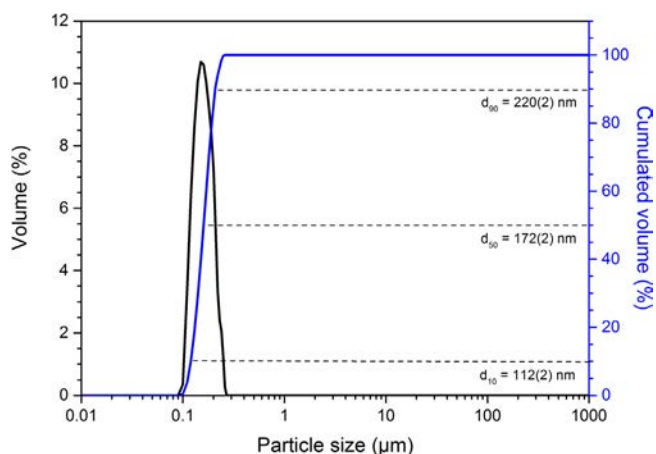


Fig. 11. Particle size distribution of the oxide microspheres ground in a tricylinder mill—in black, the frequency and in blue, the cumulative size distribution.

identified between 400 K and 600 K. The mineralization of the beads was studied, and three key temperatures were found. The average temperature for the onset of mixed oxide formation is 500 K, and a long range crystalline order starts to appear at 700 K. Lastly, it was ascertained that a single solid solution is present by 1000 K.

Once the different steps of solid solution formation were studied, a thermal treatment was established based on the previous analyses, and a batch of spherules was calcined at up to 1073 K. The sphericity of the microsphere is entirely conserved after the thermal treatment. Porosity ratios and microstructure of the beads were studied and revealed a significant (66%) open porosity ratio leading to an expanded microstructure confirmed through SEM analysis. The ability for microspheres to be broken into nanoparticles was evidenced using two complementary characterizations: the determination of a very low experimental fracture strength (2.5(5) MPa) and a monodisperse nanometric particle size distribution centered at 170 nm. This oxide microsphere precursor is thus a promising candidate for clean nanoparticle fabrication for nanomaterial applications.

To summarize, a  $Ce_{0.8}Gd_{0.2}O_{1.9}$  solid solution was selected to illustrate this new chemical route due to the use of such a compound in different scientific areas such as solid oxide fuel cells or nuclear applications. This method can now be applied to synthesis of other complex mixed oxides for materials applications which require nanostructured soft agglomerates.

## Acknowledgments

The authors thank P. Coste and M. Bataille for sample characterization; G. Jouan for SEM observations; CEA/MAR/DRCP/SE2A/LAMM for ICP measurements; L. Burylo from the UCCS for in situ XRD recordings. M. Caisso, F. Lebreton and D. Horlait are also grateful for Ph.D. and post doctoral fellowship funding by the CEA PACFA program. We acknowledge the ANKA Synchrotron Light Source for provision of beamtime at the INE beamline and for assistance in setting up the in situ XAS measurement system.

## References

- [1] R. Valiev, *Nature* 419 (2002) 887–889, <http://dx.doi.org/10.1038/419887a>.
- [2] S.L. Cumberland, K.M. Hanif, A. Javier, G.A. Khitrov, G.F. Strouse, S.M. Woessner, et al., *Chem. Mater.* 14 (2002) 1576–1584, <http://dx.doi.org/10.1021/cm010709k>.
- [3] C. Pereira, A.M. Pereira, C. Fernandes, M. Rocha, R. Mendes, M.P. Fernández-García, et al., *Chem. Mater.* 24 (2012) 1496–1504, <http://dx.doi.org/10.1021/cm300301c>.
- [4] A. Nel, T. Xia, L. Mädlar, N. Li, *Science* 311 (2006) 622–627, <http://dx.doi.org/10.1126/science.1114397>.
- [5] H. Johnston, D. Brown, A. Kermanizadeh, E. Gubbins, V. Stone, J. Controlled Release 164 (2012) 307–313, <http://dx.doi.org/10.1016/j.jconrel.2012.08.018>.
- [6] F. Gottschalk, T. Sun, B. Nowack, *Environ. Pollut.* 181 (2013) 287–300, <http://dx.doi.org/10.1016/j.envpol.2013.06.003>.
- [7] A.D. Maynard, R.J. Aitken, T. Butz, V. Colvin, K. Donaldson, G. Oberdörster, et al., *Nature* 444 (2006) 267–269, <http://dx.doi.org/10.1038/444267a>.
- [8] H. He, J.M. Vohs, R.J. Gorte, *J. Power Sources* 144 (2005) 135–140, <http://dx.doi.org/10.1016/j.jpowsour.2004.12.029>.
- [9] S.P. Jiang, S.H. Chan, *J. Mater. Sci.* 39 (2004) 4405–4439, <http://dx.doi.org/10.1023/B:JMCS.0000034135.52164.6b>.
- [10] F.S. Torknik, M. Keyanpour-Rad, A. Maghsoudipour, G.M. Choi, *Ceram. Int.* 40 (2014) 1341–1350, <http://dx.doi.org/10.1016/j.ceramint.2013.07.015>.
- [11] B. Mosqueda, J. Toyir, A. Kaddouri, P. Gélin, *Appl. Catal., B* 88 (2009) 361–367, <http://dx.doi.org/10.1016/j.apcatb.2008.11.003>.
- [12] U. Hennings, R. Reimert, *Appl. Catal., A* 325 (2007) 41–49, <http://dx.doi.org/10.1016/j.apcata.2007.02.054>.
- [13] P.K. Patro, T. Delahaye, E. Bouyer, *Solid State Ionics* 181 (2010) 1378–1386, <http://dx.doi.org/10.1016/j.ssi.2010.07.004>.
- [14] X. Liu, C.L. Martin, G. Delette, J. Laurencin, D. Bouvard, T. Delahaye, *J. Power Sources* 196 (2011) 2046–2054, <http://dx.doi.org/10.1016/j.jpowsour.2010.09.033>.
- [15] D. Warin, *J. Nucl. Sci. Technol.* 44 (2007) 410–414, <http://dx.doi.org/10.1080/1881248.2007.9711302>.
- [16] J.-P. Grouiller, S. Pillon, C. de Saint Jean, F. Varaine, L. Leyval, G. Vambenepe, et al., *J. Nucl. Mater.* 320 (2003) 163–169, [http://dx.doi.org/10.1016/S0022-3115\(03\)00184-3](http://dx.doi.org/10.1016/S0022-3115(03)00184-3).
- [17] D. Prieur, A. Jankowiah, T. Delahaye, N. Herlet, P. Dehaut, P. Blanchart, *J. Nucl. Mater.* 414 (2011) 503–507, <http://dx.doi.org/10.1016/j.jnucmat.2011.05.036>.
- [18] D. Prieur, F. Lebreton, P.M. Martin, A. Jankowiak, T. Delahaye, P. Dehaut, et al., *J. Eur. Ceram. Soc.* 32 (2012) 1585–1591, <http://dx.doi.org/10.1016/j.jeurceramsoc.2011.12.017>.
- [19] T. Delahaye, F. Lebreton, D. Horlait, N. Herlet, P. Dehaut, *J. Nucl. Mater.* 432 (2013) 305–312, <http://dx.doi.org/10.1016/j.jnucmat.2012.07.018>.
- [20] F. Lebreton, D. Prieur, A. Jankowiak, M. Tribet, C. Leorier, T. Delahaye, et al., *J. Nucl. Mater.* 420 (2012) 213–217, <http://dx.doi.org/10.1016/j.jnucmat.2011.10.016>.
- [21] P.A. Haas, 3.800.023, 1974.
- [22] G.W. Weber, R.L. Beatty, V.J. Tennery, *Processing and composition control of weak-acid-resin-derived fuel microspheres*, *Nucl. Technol.* 35 (1977) 217–226.
- [23] S. Picart, H. Mokhtari, I. Ramière, I. Jobelin, *IOP Conf. Ser. Mater. Sci. Eng.* 9 (2010) 012025, <http://dx.doi.org/10.1088/1757-899X/9/1/012025>.
- [24] M.S. Wilson, A. Delariva, F.H. Garzon, *J. Mater. Chem.* 21 (2011) 7418–7424, <http://dx.doi.org/10.1039/C1JM10529A>.
- [25] E. Remy, S. Picart, S. Grandjean, T. Delahaye, N. Herlet, P. Allegri, et al., *J. Eur. Ceram. Soc.* 32 (2012) 3199–3209, <http://dx.doi.org/10.1016/j.jeurceramsoc.2012.04.011>.
- [26] G.T. Seaborg, *Radiochim. Acta* 61 (1993) 115–222.
- [27] J.R. Carjaval, *Powder Diffr.* XV IUCr Congr. (1990).
- [28] A. Le Bail, *Powder Diffr.* 20 (2005) 316–326, <http://dx.doi.org/10.1154/1.2135315>.
- [29] J.I. Langford, *J. Appl. Crystallogr.* 11 (1978) 10–14, <http://dx.doi.org/10.1107/S0021889878012601>.
- [30] J. Rothe, M.A. Denecke, K. Dardenne, T. Fanghanel, *Radiochim. Acta* 94 (2006) 691–696.
- [31] K. Dardenne, B. Brendebach, M.A. Denecke, X. Liu, J. Rothe, T. Vitova, J. Phys. Conf. Ser. 190 (2009) 012037–012037/4, <http://dx.doi.org/10.1088/1742-6596/190/1/012037>.
- [32] V. Magnien, D.R. Neuville, L. Cormier, J. Roux, J.-L. Hazemann, D. de Ligny, et al., *Geochim. Cosmochim. Acta* 72 (2008) 2157–2168, <http://dx.doi.org/10.1016/j.gca.2008.02.007>.
- [33] D.R. Neuville, L. Cormier, V. Montouillout, P. Florian, F. Millot, J.-C. Rifflet, et al., *Am. Mineral.* 93 (2008) 1721–1731, <http://dx.doi.org/10.2138/am.2008.2867>.
- [34] M. Newville, *J. Synchrotron Radiat.* 8 (2001) 322–324, <http://dx.doi.org/10.1107/S0909049500016964>.
- [35] B. Ravel, M. Newville, *J. Synchrotron Radiat.* 12 (2005) 537–541, <http://dx.doi.org/10.1107/S0909049505012719>.
- [36] O.T. Sørensen, *J. Solid State Chem.* 18 (1976) 217–233, [http://dx.doi.org/10.1016/0022-4596\(76\)90099-2](http://dx.doi.org/10.1016/0022-4596(76)90099-2).
- [37] A. Kossov, A.I. Frenkel, Q. Wang, E. Wachtel, I. Lubomirsky, *Adv. Mater.* 22 (2010) 1659–1662, <http://dx.doi.org/10.1002/adma.200902041>.
- [38] V. Grover, A.K. Tyagi, *Mater. Res. Bull.* 39 (2004) 859–866, <http://dx.doi.org/10.1016/j.materresbull.2004.01.007>.
- [39] B. Choudhury, A. Choudhury, *Curr. Appl. Phys.* 13 (2013) 217–223, <http://dx.doi.org/10.1016/j.cap.2012.07.014>.
- [40] L. Minervini, M.O. Zacate, R.W. Grimes, *Solid State Ionics* 116 (1999) 339–349, [http://dx.doi.org/10.1016/S0167-2738\(98\)00359-2](http://dx.doi.org/10.1016/S0167-2738(98)00359-2).
- [41] D. Horlait, L. Claparède, N. Clavier, S. Szenknect, N. Dacheux, J. Ravaux, et al., *Inorg. Chem.* 50 (2011) 7150–7161, <http://dx.doi.org/10.1021/ic200751m>.
- [42] J.R. McBride, K.C. Hass, B.D. Poindexter, W.H. Weber, *J. Appl. Phys.* 76 (1994) 2435–2441, <http://dx.doi.org/10.1063/1.357593>.
- [43] M.G. Chourashiya, J.Y. Patil, S.H. Pawar, L.D. Jadhav, *Mater. Chem. Phys.* 109 (2008) 39–44, <http://dx.doi.org/10.1016/j.matchemphys.2007.10.028>.
- [44] L. Claparède, Influence de paramètres physico-chimiques et microstructuraux sur la dissolution d'oxydes mixtes Th<sub>1-x</sub>Ce<sub>x</sub>O<sub>2</sub>, Th<sub>1-x</sub>Ce<sub>x</sub>O<sub>2</sub> et Ce<sub>1-x</sub>Nd<sub>x</sub>O<sub>2-x/2</sub>, Montpellier 2, 2011.
- [45] M. Durazzo, F.B.V. Oliveira, E.F. Urano de Carvalho, H.G. Riella, *J. Nucl. Mater.* 400 (2010) 183–188, <http://dx.doi.org/10.1016/j.jnucmat.2010.03.001>.
- [46] M. Durazzo, A.M. Saliba-Silva, E.F.U. de Carvalho, H.G. Riella, *J. Nucl. Mater.* 405 (2010) 203–205, <http://dx.doi.org/10.1016/j.jnucmat.2010.08.002>.
- [47] D. Horlait, A. Feledziak, F. Lebreton, N. Clavier, D. Prieur, N. Dacheux, et al., *J. Nucl. Mater.* 441 (2013) 40–46, <http://dx.doi.org/10.1016/j.jnucmat.2013.05.024>.
- [48] Y. Takahashi, H. Sakami, M. Nomura, *Anal. Chim. Acta* 468 (2002) 345–354, [http://dx.doi.org/10.1016/S0003-2670\(02\)00709-2](http://dx.doi.org/10.1016/S0003-2670(02)00709-2).
- [49] Horiba Jobin Yvon, *Raman and Data Analysis—Raman Spectroscopy for Analysis and Monitoring*, n.d.
- [50] A. Banerji, V. Grover, V. Sathe, S.K. Deb, A.K. Tyagi, *Solid State Commun.* 149 (2009) 1689–1692, <http://dx.doi.org/10.1016/j.ssc.2009.06.045>.
- [51] S. Yamazaki, T. Matsui, T. Ohashi, Y. Arita, *Solid State Ionics* 136–137 (2000) 913–920, [http://dx.doi.org/10.1016/S0167-2738\(00\)00569-5](http://dx.doi.org/10.1016/S0167-2738(00)00569-5).
- [52] A. Nakajima, A. Yoshihara, M. Ishigame, *Phys. Rev. B: Condens. Matter* 50 (1994) 13297–13307, <http://dx.doi.org/10.1103/PhysRevB.50.13297>.
- [53] V.G. Keramidis, W.B. White, *J. Am. Ceram. Soc.* 57 (1974) 22–24, <http://dx.doi.org/10.1111/j.1151-2916.1974.tb11355.x>.
- [54] T. Ohashi, S. Yamazaki, T. Tokunaga, Y. Arita, T. Matsui, T. Harami, et al., *Solid State Ionics* 113–115 (1998) 559–564, [http://dx.doi.org/10.1016/S0167-2738\(98\)00322-1](http://dx.doi.org/10.1016/S0167-2738(98)00322-1).
- [55] F. Zhang, S.-W. Chan, J.E. Spanier, E. Apak, Q. Jin, R.D. Robinson, et al., *Appl. Phys. Lett.* 80 (2002) 127–129, <http://dx.doi.org/10.1063/1.1430502>.
- [56] B.P. Mandal, V. Grover, M. Roy, A.K. Tyagi, *J. Am. Ceram. Soc.* 90 (2007) 2961–2965, <http://dx.doi.org/10.1111/j.1551-2916.2007.01826.x>.
- [57] B.P. Mandal, M. Roy, V. Grover, A.K. Tyagi, *J. Appl. Phys.* 103 (2008) 033506, <http://dx.doi.org/10.1063/1.2837042>.
- [58] E. Remy, Étude de la synthèse de sphères d'oxyde d'actinides et/ou de lanthanides et de leur aptitude à la céramisation, Université de Montpellier 2, 2013.

## Repository KITopen

Dies ist ein Postprint/begutachtetes Manuskript.

Empfohlene Zitierung:

Caisso, M.; Lebreton, F.; Horlait, D.; Picart, S.; Martin, P. M.; Bes, R.; Renard, C.; Roussel, P.; Neuville, D. R.; Dardenne, K.; Rothe, J.; Delahaye, T.; Ayrat, A.

[Nanostructured gadolinium-doped ceria microsphere synthesis from ion exchange resin: Multi-scale in-situ studies of solid solution formation](#)

2014. Journal of solid state chemistry, 218, 155–163.

[doi:10.5445/IR/110098329](https://doi.org/10.5445/IR/110098329)

Zitierung der Originalveröffentlichung:

Caisso, M.; Lebreton, F.; Horlait, D.; Picart, S.; Martin, P. M.; Bes, R.; Renard, C.; Roussel, P.; Neuville, D. R.; Dardenne, K.; Rothe, J.; Delahaye, T.; Ayrat, A.

[Nanostructured gadolinium-doped ceria microsphere synthesis from ion exchange resin: Multi-scale in-situ studies of solid solution formation](#)

2014. Journal of solid state chemistry, 218, 155–163.

[doi:10.1016/j.jssc.2014.06.028](https://doi.org/10.1016/j.jssc.2014.06.028)